



K2-19b and c are in a 3:2 Commensurability but out of Resonance: A Challenge to Planet Assembly by Convergent Migration

Erik A. Petigura¹ , John Livingston^{2,14} , Konstantin Batygin³, Sean M. Mills⁴ , Michael Werner⁵, Howard Isaacson^{6,7} , Benjamin J. Fulton⁸ , Andrew W. Howard⁴ , Lauren M. Weiss^{9,15} , Néstor Espinoza^{10,16} , Daniel Jontof-Hutter¹¹ , Avi Shporer¹² , Daniel Bayliss^{13,17} , and S. C. C. Barros¹³

¹ Department of Physics & Astronomy, University of California Los Angeles, Los Angeles, CA 90095, USA; petigura@astro.ucla.edu

² Department of Astronomy, University of Tokyo, 7-3-1 Hongo, Bunkyo-ku, Tokyo 113-0033, Japan

³ Division of Geological and Planetary Sciences, California Institute of Technology, Pasadena CA 91125, USA

⁴ Cahill Center for Astrophysics, California Institute of Technology, Pasadena CA 91125, USA

⁵ Jet Propulsion Laboratory, California Institute of Technology, Pasadena, CA 91109, USA

⁶ Department of Astronomy, University of California Berkeley, Berkeley CA 94720, USA

⁷ University of Southern Queensland, Toowoomba, QLD 4350, Australia

⁸ IPAC-NASA Exoplanet Science Institute Pasadena, CA 91125, USA

⁹ Institute for Astronomy, University of Hawaii at Manoa, Honolulu, HI 96822, USA

¹⁰ Max-Planck-Institut für Astronomie, Königstuhl 17, D-69117 Heidelberg, Germany

¹¹ Department of Physics, University of the Pacific, Stockton, CA 95211, USA

¹² Department of Physics and Kavli Institute for Astrophysics and Space Research, Massachusetts Institute of Technology, Cambridge, MA 02139, USA

¹³ Instituto de Astrofísica e Ciências do Espaço, Universidade do Porto, CAUP, Rua das Estrelas, PT4150-762 Porto, Portugal

Received 2019 April 6; revised 2019 October 10; accepted 2019 October 24; published 2019 December 10

Abstract

K2-19b and c were among the first planets discovered by NASA’s *K2* mission and together stand in stark contrast with the physical and orbital properties of the solar system planets. The planets are between the size of Uranus and Saturn at $7.0 \pm 0.2 R_{\oplus}$ and $4.1 \pm 0.2 R_{\oplus}$, respectively, and reside a mere 0.1% outside the nominal 3:2 mean-motion resonance. They represent a different outcome of the planet formation process than the solar system, as well as the vast majority of known exoplanets. We measured the physical and orbital properties of these planets using photometry from *K2*, *Spitzer*, and ground-based telescopes, along with radial velocities from Keck/HIRES. Through a joint photodynamical model, we found that the planets have moderate eccentricities of $e \approx 0.20$ and well-aligned apsides $\Delta\varpi \approx 0^\circ$. The planets occupy a strictly nonresonant configuration: the resonant angles circulate rather than librate. This defies the predictions of standard formation pathways that invoke convergent or divergent migration, both of which predict $\Delta\varpi \approx 180^\circ$ and eccentricities of a few percent or less. We measured masses of $M_{p,b} = 32.4 \pm 1.7 M_{\oplus}$ and $M_{p,c} = 10.8 \pm 0.6 M_{\oplus}$. Our measurements, with 5% fractional uncertainties, are among the most precise of any sub-Jovian exoplanet. Mass and size reflect a planet’s core/envelope structure. Despite having a relatively massive core of $M_{\text{core}} \approx 15 M_{\oplus}$, K2-19b is envelope-rich, with an envelope mass fraction of roughly 50%. This planet poses a challenge to standard models of core-nucleated accretion, which predict that cores $\gtrsim 10 M_{\oplus}$ will quickly accrete gas and trigger runaway accretion when the envelope mass exceeds that of the core.

Unified Astronomy Thesaurus concepts: Exoplanet astronomy (486); Exoplanet dynamics (490); Exoplanet formation (492); Exoplanet evolution (491); Extrasolar gas giants (509); Exoplanet structure (495); Radial velocity (1332)

Supporting material: machine-readable tables

1. Introduction

While a perennial quest in exoplanet astronomy is the discovery and characterization of ever more “Earth-like” worlds, our understanding of planet formation is best informed by the full diversity of planets around other stars. Thanks to the rapidly growing census of extrasolar planets, we may now study the diverse outcomes of planet formation processes beyond those that occurred in the solar system. The K2-19 system is one such outcome.

The system hosts three known planets. Armstrong et al. (2015) initially reported K2-19b and c based on photometry collected by the *Kepler Space Telescope* operating in its *K2*

mode (Howell et al. 2014). K2-19b has an orbital period of 7.9 days and has a radius of $7.0 R_{\oplus}$, between the size of Uranus and Saturn. K2-19 c has an orbital period of 11.9 days and a radius of $4.1 R_{\oplus}$. While K2-19 c is similar in size to the solar system ice giants, aspects of its bulk composition, such as ice fraction, may be quite different due its close-in orbit. As techniques to correct for *K2* systematics improved, Sinukoff et al. (2016) detected a third planet, K2-19d, a $1.2 R_{\oplus}$ planet on a 2.5 day orbit.

In this paper, we focus on K2-19b and c, which reside just outside the nominal 3:2 mean-motion resonance. While Armstrong et al. (2015) detected transit-timing variations (TTVs) within the *K2* data set, the relatively short 80 day baseline resulted in significant uncertainties in the TTV model. Several groups have subsequently observed transits of K2-19b from the ground in order to better constrain the TTV model (Armstrong et al. 2015; Barros et al. 2015; Narita et al. 2015). However, to date, there have been no successful recoveries

¹⁴ JSPS Fellow.

¹⁵ Parrent Postdoctoral Fellow.

¹⁶ Bernoulli Fellow IAU-Gruber Fellow.

¹⁷ Observatoire Astronomique de l’Université de Genève, 51 ch. des Maillettes, 1290 Versoix, Switzerland.

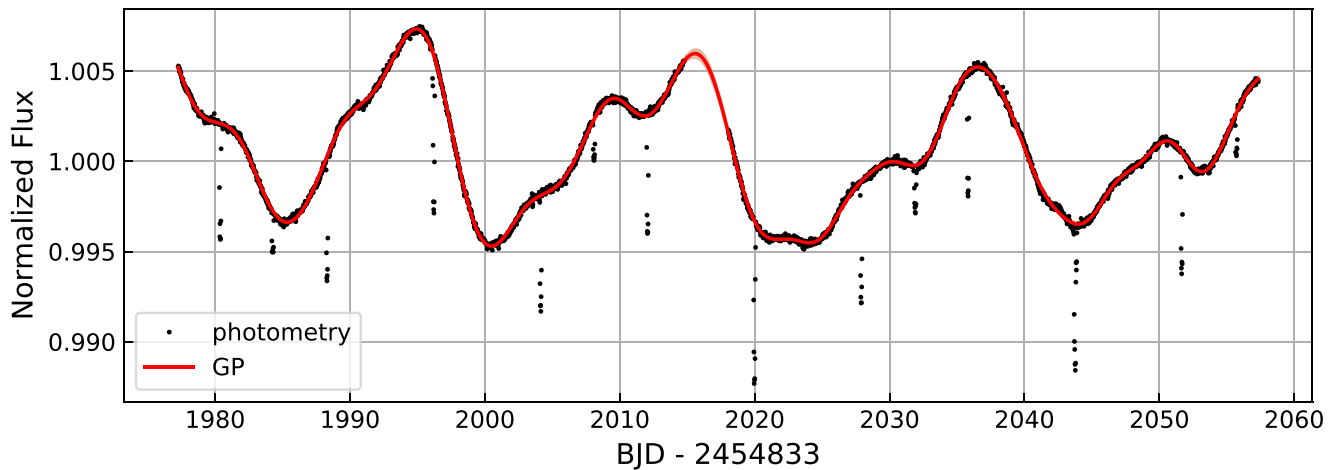


Figure 1. Photometry from *K2* after removing instrument systematics showing $\approx 1\%$ periodic variability with $P \approx 20$ days (see Section 2.1). The red line is our Gaussian process fit to the photometry, which informs the adopted noise model in our RV analysis (see Section 4.1).

of the K2-19 c transit, which has contributed to lingering uncertainty in the TTV solution.

In parallel, several groups have obtained radial velocity (RV) measurements of K2-19 in order to directly constrain the planet masses through stellar reflex motion (Dai et al. 2016; Nespral et al. 2017). A key challenge to these efforts is that at $V = 13.0$ mag, K2-19 is near the faint limit of most current RV facilities. In addition, the star exhibits significant RV variability due to spot modulation, which must be disentangled from the planetary signals.

In this work, we present the results of a coordinated observational campaign to characterize K2-19b and c, using both TTVs and RVs. We describe our photometry in Section 2 and our RVs in Section 3. Our photometric data set includes two *Spitzer* observations for each planet. Our *Spitzer* observations of the K2-19 c transits are significant in that they are the first *K2* and help to reduce uncertainties in the TTV solution. We perform a photodynamical analysis in Section 4, which yields the most precise constraints on the masses and orbits of these two planets to date. In Sections 5–7 we assess the bulk composition of these planets, their dynamical evolution, and possible formation pathways.

2. Photometric Observations

2.1. *K2* Photometry

The *Kepler Space Telescope* observed K2-19 from 2014 May 30 to 2014 August 21 during campaign 1 of its *K2* mission. The photometry contain large systematics due to pointing drifts of ~ 1 pixel that occur on ~ 6 hr timescales. We used the EVEREST2.0 package to correct for these systematics (Luger et al. 2018), and the corrected light curve is shown in Figure 1. There is clear periodic variability with $P \approx 20$ days with a peak-to-trough amplitude of 1% due to rotation-induced spot modulation. Figure 2 is a zoomed in view of individual transits, some of which are overlapping.

2.2. *Spitzer* Photometry

The *K2* data alone samples only a small fraction of the multiyear TTV signal. We used the *Spitzer Space Telescope* to observe two additional transits of K2-19b and K2-19 c to better sample this signal. Planet b observations were conducted on 2017

April 23 and 2017 September 5; planet c observations were conducted on 2016 October 4 and 2017 April 8.¹⁸

To plan the first set of *Spitzer* observations, we consulted the transit times predicted by Barros et al. (2015; S. Barros 2019, private communication). Because our first *Spitzer* observation of K2-19b was two years after the last transit used in the Barros et al. (2015) model, there was considerable timing uncertainty. We observed for 12 hr to reliably catch the 3.5 hr transit. There was even more timing uncertainty for K2-19 c, which had not been observed since 2014, and we scheduled a 27 hr observing sequence.

When planning our second set of *Spitzer* observations, we constructed a preliminary TTV model with plausible values for the planet masses and eccentricity. Having incorporated the first set of observations, there was less uncertainty in the transit times of K2-19b and c, requiring only 7 and 9 hr observing sequences, respectively.

We used IRAC channel 2 ($4.5 \mu\text{m}$) because the instrumental systematics due to intrapixel sensitivity variations are smaller than in channel 1 ($3.6 \mu\text{m}$; Ingalls et al. 2012). We used 2 s exposures to optimize the integration efficiency while remaining in the linear regime of the detector. We extracted photometry from the *Spitzer* data using circular apertures. As described in Livingston et al. (2019), we selected the aperture size ($r = 2.2$ pixels) that minimized the combined uncorrelated (white) and correlated (red) noise, as measured by the standard deviation and β factor (Pont et al. 2006; Winn et al. 2008). We resampled the light curve into 60 s integrations which yields improved systematic modeling without significantly altering the transit profile (Benneke et al. 2017).

Following standard practice, we modeled the *Spitzer* systematics and transit profile simultaneously. Using the pixel-level decorrelation (PLD) method of Deming et al. (2015), we constructed our systematic model from a linear combination of the nine pixel-level light curves from a 3×3 pixel grid centered on the star. For K2-19b and c, we modeled each set of two transits simultaneously and shared all transit parameters except for the transit mid-times $T_{c,i}$. We used a quadratic limb-darkening parameterization and physically motivated priors (Claret et al. 2012; Kipping 2013). In

¹⁸ All observations were carried out under GO program 13052 (PI: M. Werner).

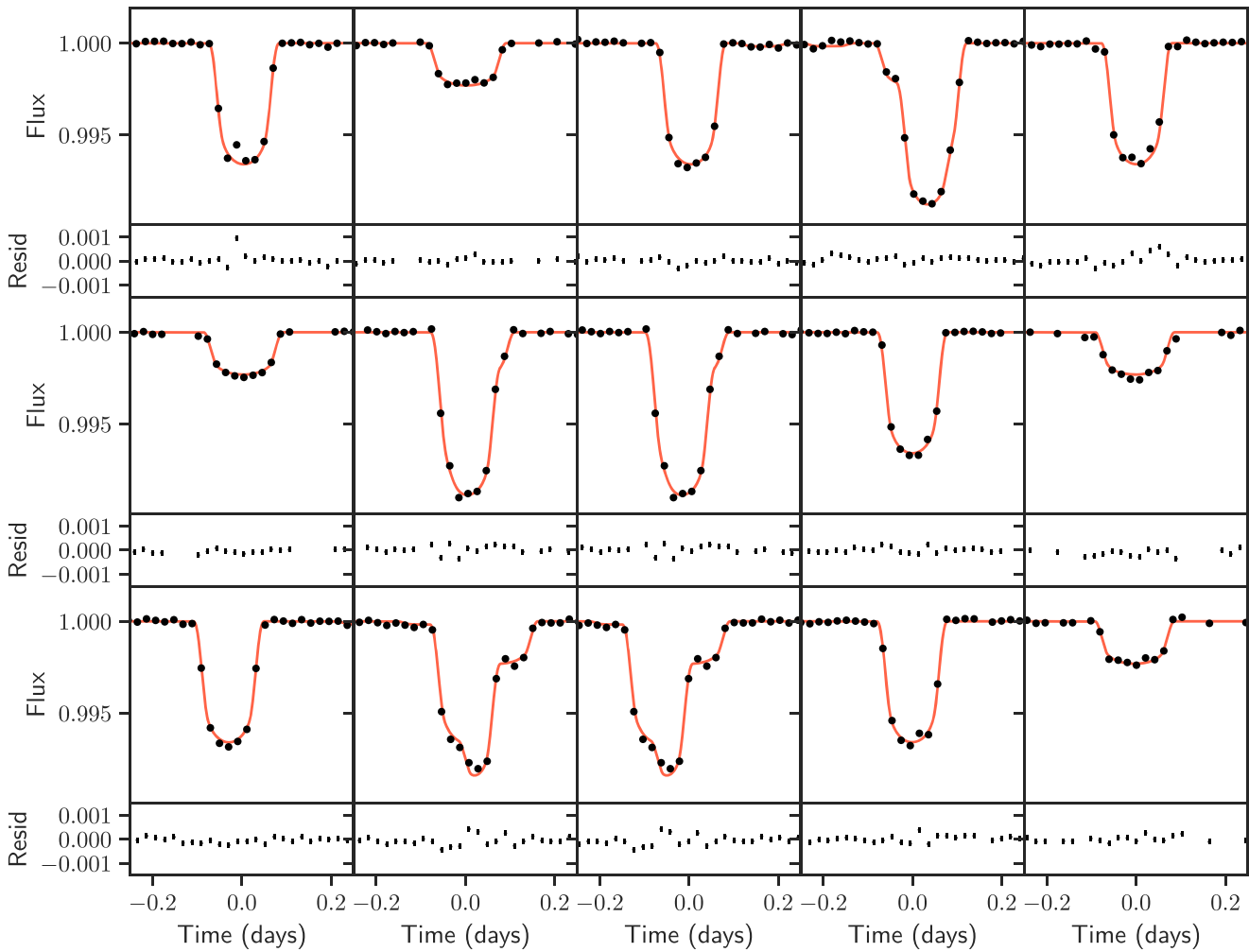


Figure 2. Black circles show the detrended *K2* photometry around the transits. Several overlapping transits are observed. The maximum a posteriori model is shown as the orange line and the residuals to this model are shown below. Increased scatter during transit due to spot crossing events are observed during some transits (see Section 4.2).

summary, our modeling of each planet involved 28 free parameters: nine PLD coefficients for each data set, a white noise term for each data set, two transit midpoints $T_{c,i}$, the orbital period P , the planet–star radius ratio R_p/R_* , the scaled semimajor axis a/R_* , the impact parameter b , and the limb-darkening parameters q_1 and q_2 .

We explored the range of coefficients allowed by our data using the affine-invariant Markov Chain Monte Carlo (MCMC) sampler of Goodman & Weare (2010). We initialized 100 walkers and allowed them to evolve for $N_{\text{steps}} = 10,000$ steps. We visually inspected the trace plots and discarded the first 5000 steps of burn-in. We assessed the convergence by computing the autocorrelation length τ for each chain. We computed the mean value of τ for all 100 chains for each parameter, and found that $N_{\text{steps}}/\tau \geq 38$ for all chains. Our corrected light curves had an rms scatter of ~ 400 ppm on a 40 minute timescales. The *Spitzer* photometry and best-fit transit models are shown Figure 3. The derived transit times are listed in Table 1.

2.3. Ground-based Photometry

We also included several transit times of K2-19b measured using ground-based facilities. Three were drawn from Narita et al. (2015). We also observed a transit on 2017 June 5 with

the 1 m telescope of the Las Cumbres Observatory network (LCO; Brown et al. 2013), located at the South African Astronomical Observatory. We performed bias, dark, and flat-field corrections using the standard LCOGT pipeline (McCully et al. 2018). We then performed aperture photometry on K2-19 and 10 comparison stars having similar 2MASS colors and performed differential photometry to remove instrumental and atmospheric effects. We modeled the transit using both white and correlated noise models and found that the white noise mode was preferred. The light curve and transit fit are shown in Figure 4. The rms scatter in the residuals is ≈ 300 ppm per 40 minutes interval.

3. RV Observations

We obtained 51 spectra of K2-19 using the High Resolution Echelle Spectrometer (HIRES; Vogt et al. 1994) on the 10 m Keck I telescope between 2015 February 5 and 2017 December 26. We collected spectra through an iodine cell mounted directly in front of the spectrometer slit. The iodine cell imprints a dense forest of absorption lines which serve as a wavelength reference. We also obtained a “template” spectrum without iodine.

At $V = 13.0$ mag, K2-19 is a challenging RV target for Keck/HIRES. We aimed to achieve a consistent signal-to-noise

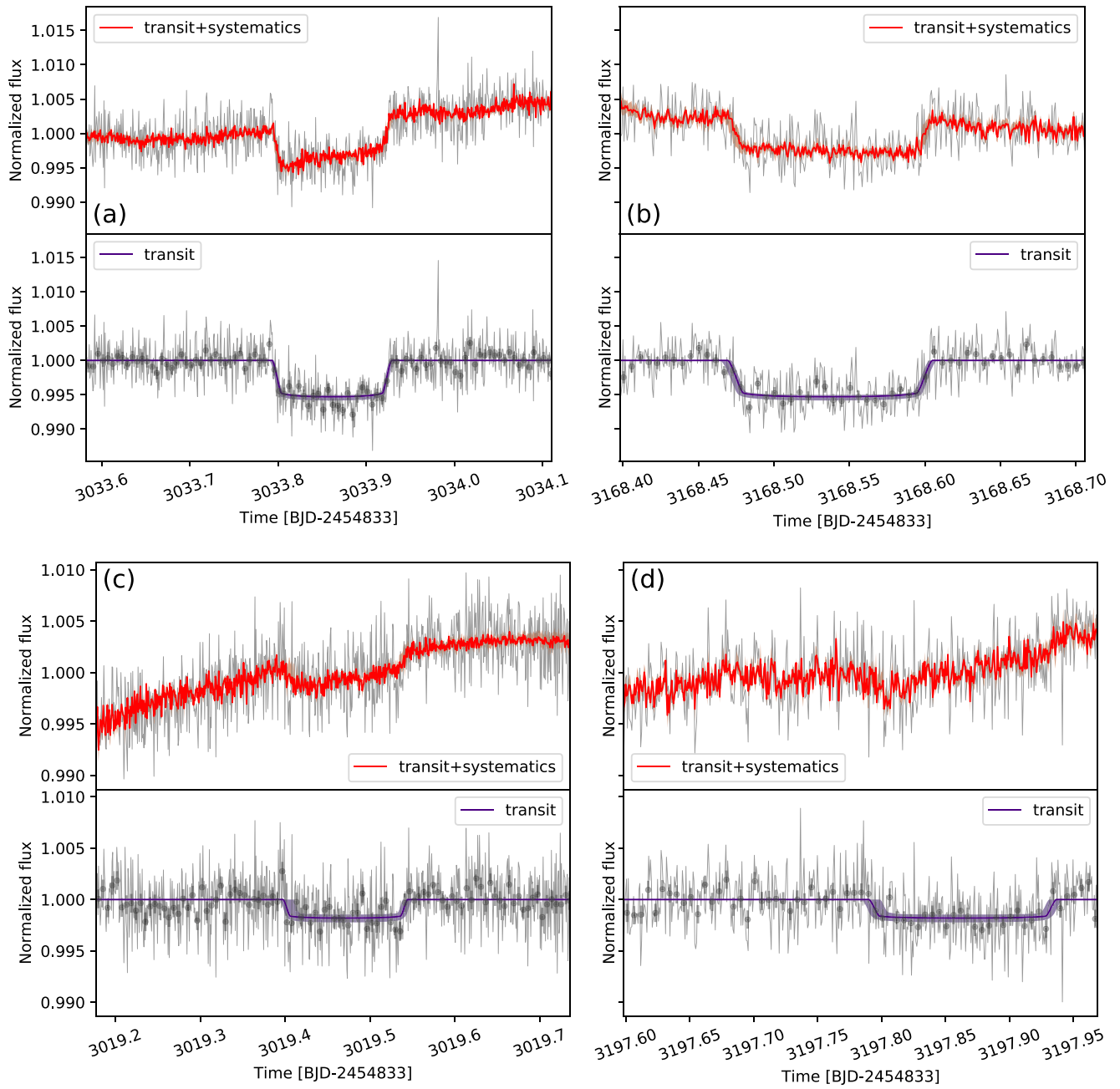


Figure 3. Transits of K2-19b and c observed by *Spitzer* in the $4.5\ \mu\text{m}$ IRAC channel along with our simultaneous modeling of the instrumental systematics and transit profiles (see Section 2.2). Panel (a) shows the transit of K2-19b with a transit number $i = 133$, where $i = 0$ corresponds to the first *K2* transit. In the top subpanel, we show the raw light curve (gray), the maximum a posteriori (MAP) transit/systematic model (red), and the 95% credible models (light red band). In the bottom subpanel, we show the MAP corrected photometry (gray) and transit model (purple). The 95% credible models are shown with the purple band. Panel (b): same as (a) but for the second *Spitzer* observation of K2-19b ($i = 150$). Panel (c): same as (a) but for the first *Spitzer* observation of K2-19c ($i = 87$). Panel (d): same as (a) but for the second *Spitzer* observation of K2-19c ($i = 102$).

ratio (S/N) of 100 per reduced pixel at $5500\ \text{\AA}$ using an exposure meter. However, various throughput losses due to poor/variable seeing and cirrus clouds sometimes resulted in lower than desired S/N. Our spectra have per pixel S/N ranging from 53 to 108.

RVs were determined using standard procedures of the California Planet Search (Howard et al. 2010) including forward modeling of the stellar and iodine spectra convolved with the instrumental response (Marcy & Butler 1992; Valenti et al. 1995). The measurement uncertainty of each RV point is derived from the uncertainty on the mean RV of the ~ 700

spectral chunks used in the RV pipeline and ranges from 1.9 to $3.8\ \text{m s}^{-1}$. Table 2 lists the RVs and uncertainties.

4. TTV and RV Modeling

Here, we describe our modeling of both the photometric and RV data sets. In Section 4.1, we perform a Keplerian analysis of the RVs only. We observe quasiperiodic RV variability due to rotating starspots, which we model with a Gaussian process. Section 4.2 describes our photodynamical analysis that incorporates constraints from both photometry and RVs. This analysis yields tighter constraints on the properties of K2-19b

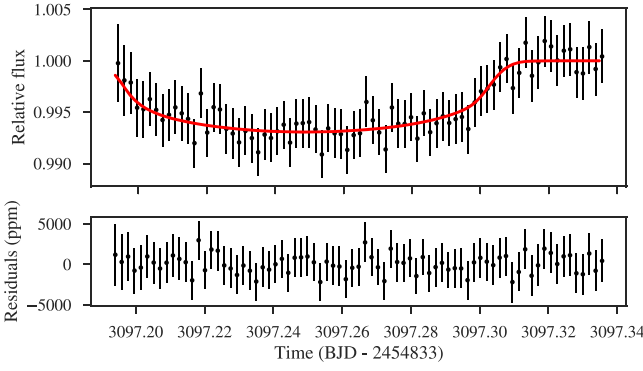


Figure 4. Top panel: black points show the relative photometry of K2-19 observed by LCO on 2017 June 5 during the transit of K2-19b (see Section 2.3). The red line is the best-fit transit model and the bottom panel shows the residuals to the fit.

Table 1
Transit Times

Planet	Transit	Instrument	T_c days	$\sigma(T_c)$ days	Notes
K2-19b	30	FLWO	2218.0041	0.0022	B
K2-19b	34	TRAPPIST	2249.6955	0.0014	B
K2-19b	41	MuSCAT	2305.1505	0.0014	B
K2-19b	133	Spitzer	3033.8604	0.0009	A
K2-19 c	87	Spitzer	3019.4774	0.0074	A
K2-19b	141	LCO	3097.2502	0.0024	A
K2-19b	150	Spitzer	3168.5368	0.0014	A
K2-19 c	102	Spitzer	3197.8645	0.0059	A

Note. Following a convention from the *Kepler* mission, times are given in $\text{BJD}_{\text{TBD}} - 2454833$. Notes—A: this work; B: Narita et al. (2015).

(This table is available in machine-readable form.)

Table 2
Radial Velocities

Time days	RV (m s^{-1})	$\sigma(\text{RV})$ (m s^{-1})	S_{HK}
2225.996346	-8.92	2.69	0.358
2229.058283	-14.53	2.84	0.328
2346.849965	-11.35	1.98	0.181
2366.792920	-0.21	2.04	0.247
2367.829151	-9.39	3.37	0.221
2368.814357	-14.07	2.20	0.182
2370.809676	-18.62	2.13	0.221
2374.805352	6.22	3.15	0.195
2375.803685	2.94	2.18	0.249
2376.797458	-14.34	2.12	0.269

Note. Radial velocities and uncertainties for K2-19 (see Section 3). Times are given in $\text{BJD}_{\text{TBD}} - 2454833$. We also provide the Mount Wilson S_{HK} activity index (Vaughan et al. 1978), which is measured to 1% precision.

(This table is available in its entirety in machine-readable form.)

and c and the parameters listed in Table 3 constitute our adopted system parameters.

While the photodynamical analysis yields smaller uncertainties, we present the RV-only analysis for the following reasons:

- (1) The RVs provide sensitivity to nontransiting planets that could compromise the accuracy of the photodynamical model.
- (2) RV variability from rotating starspots is comparable in

Table 3
K2-19 System Parameters

Parameter	Value	Notes
Stellar Parameters		
T_{eff} (K)	5322 ± 100	A
$\log g$ (dex)	4.51 ± 0.08	A
[Fe/H] (dex)	0.06 ± 0.05	A
K (mag)	11.2 ± 0.03	B
π_* (mas)	3.42 ± 0.06	C
Photodynamical Analysis		
M_* (M_{\odot})	0.88 ± 0.03	D, E
R_* (R_{\odot})	0.82 ± 0.03	D, E
q_1	0.4 ± 0.1	D
q_2	0.3 ± 0.2	D
P_b (days)	7.9222 ± 0.0001	D
$T_{c,b}$ (BJD-2454833)	2027.9023 ± 0.0002	D
$\sqrt{e_b} \cos \omega_b$	0.02 ± 0.06	D
$\sqrt{e_b} \sin \omega_b$	-0.44 ± 0.04	D
i_b (deg)	91.5 ± 0.1	D
Ω_b (deg)	0 (fixed)	D
$R_{p,b}/R_*$	0.0777 ± 0.0006	D
$M_{p,b}$ (M_{\oplus})	32.4 ± 1.7	D, F
P_c (days)	11.8993 ± 0.0008	D
$T_{c,c}$ (BJD-2454833)	2020.0007 ± 0.0004	D
$\sqrt{e_c} \cos \omega_c$	0.04 ± 0.04	D
$\sqrt{e_c} \sin \omega_c$	-0.46 ± 0.03	D
i_c (deg)	91.1 ± 0.1	D
Ω_c (deg)	-7.4 ± 0.8	D
$R_{p,c}/R_*$	0.0458 ± 0.0004	D
$M_{p,c}$ (M_{\oplus})	10.8 ± 0.6	D, F
P_d (days)	2.5081 ± 0.0002	D
$T_{c,d}$ (BJD-2454833)	2021.0726 ± 0.0018	D
$\sqrt{e_d} \cos \omega_d$	0 (fixed)	D
$\sqrt{e_d} \sin \omega_d$	0 (fixed)	D
i_d (deg)	90.8 ± 0.7	D
Ω_d (deg)	0 (fixed)	D
$R_{p,d}/R_*$	0.0124 ± 0.0004	D
$M_{p,d}$ (M_{\oplus})	< 10	D, F
Derived Parameters		
$R_{p,b}$ (R_{\oplus})	7.0 ± 0.2	G
$R_{p,d}$ (R_{\oplus})	1.11 ± 0.05	G
$R_{p,c}$ (R_{\oplus})	4.1 ± 0.2	G
e_b	0.20 ± 0.03	G
e_c	0.21 ± 0.03	G
$\Delta\omega$ (deg)	2 ± 2	G
$f_{\text{env},b}$ (%)	44 ± 3	H
$f_{\text{env},c}$ (%)	14 ± 1	H
$M_{\text{core},b}$ (M_{\oplus})	18 ± 1	H
$M_{\text{core},c}$ (M_{\oplus})	9.4 ± 0.5	H

Note. A: Brewer et al. (2016). B: 2MASS (Skrutskie et al. 2006). C: *Gaia* DR2 (Gaia Collaboration et al. 2018). D: input parameters into photodynamical model, see Section 4.2. E: we imposed Gaussian priors on M_* and R_* using the methodology described in Fulton & Petigura (2018) that incorporated A, B, and C. F: based on our RV analysis (Section 4.1), we imposed the following Gaussian priors on planet masses: $M_{p,b} = 33 \pm 5 M_{\oplus}$, $M_{p,c} = 0 \pm 10 M_{\oplus}$, and $M_{p,d} = 0.0 \pm 3.2 M_{\oplus}$. G: derived from the posterior samples of D. H: derived from the planet mass & radius constraints along with the core-envelope models of Lopez & Fortney (2014). See Section 5 for further details.

amplitude to that due to K2-19b and may account for discrepancies between previously published mass measurements. (3) The two analyses demonstrate the relative strengths

and weaknesses of the TTV and RV techniques as probes of the properties of the K2-19 system.

4.1. Keplerian RV Modeling

We analyzed the RV timeseries using the open source package RadVel (Fulton et al. 2018). RadVel facilitates maximum a posteriori (MAP) model fitting and parameter estimation via MCMC. In general, a Keplerian RV signal may be described by the orbital period P , time of inferior conjunction T_c , eccentricity e , argument of periastron ω , and Doppler semiamplitude K . We included K2-19b, c, and d in our model with zero eccentricity. For planets b and c we fixed P and T_c to the mean value as determined by the *K2* and *Spitzer* photometry. For planet d, we fixed P and T_c to the Sinukoff et al. (2016) ephemeris. While the planets do not have strictly linear ephemerides, we confirmed that the errors introduced by this simplification are negligible after performing the photodynamical analysis described in Section 4.2. In our preliminary fitting, we found that models with a linear acceleration term dv/dt were favored by the Bayesian Information Criterion (BIC; Schwarz 1978) with $\Delta\text{BIC} = -15$. In our subsequent modeling, described below, we found $dv/dt = 5.9 \pm 2.4 \text{ m s}^{-1} \text{ yr}^{-1}$.

The K2-19 photometry shows clear spot modulation (see Figure 1), which can introduce correlated noise into the RV timeseries. We estimated the amplitude of this noise using the FF' method of Aigrain et al. (2012):

$$\begin{aligned} \Delta\text{RV} &\sim FF'R_*/f \\ &\sim (0.5\%)(1\%/5 \text{ days})(0.82 R_\odot)/(1\%) \\ &\sim 7 \text{ m s}^{-1}. \end{aligned}$$

Here, F is the fractional flux variation, F' is its time derivative, and f is the maximum flux decrement due to spots. This noise source is quasiperiodic as spots rotate with the stellar photosphere and also evolve with time. Numerous prior studies have modeled spot noise with quasiperiodic Gaussian processes including Haywood et al. (2014), Grunblatt et al. (2015), and others. We used the following quasiperiodic kernel that specifies the covariance between the i and j measurements:

$$\begin{aligned} C_{ij} &= \eta_1^2 \exp \left[-\frac{(t_i - t_j)^2}{\eta_2^2} - \frac{1}{2\eta_4^2} \sin^2 \frac{\pi(t_i - t_j)}{\eta_3} \right] \\ &+ [\sigma_i^2 + \sigma_{jit}^2] \delta_{ij}. \end{aligned}$$

Here, η_1 is the covariance amplitude, η_2 is the exponential decay length, η_3 sets the period, η_4 sets the relative importance of the exponential decay part of the kernel, and δ_{ij} is the Kronecker delta function. We trained the GP on the *K2* photometry and found $\eta_1 = 0.4\% \pm 0.1\%$, $\eta_2 = 34 \pm 5$ days, $\eta_3 = 20.4 \pm 0.3$ days, and $\eta_4 = 0.49 \pm 0.06$. Our value for η_3 is consistent with our visual assessment of the stellar rotation period of $P \approx 20$ days.

We then modeled the RVs using the GP-based likelihood (see RadVel documentation for details). We imposed Gaussian priors on η_2 , η_3 , and η_4 based on our photometric modeling described above. In summary, our RV model had the following free parameters: $\{K_1, K_2, K_3, dv/dt, \eta_1, \eta_2, \eta_3, \eta_4, \gamma, \sigma_{jit}\}$.

Figure 5 shows the MAP model. We derived uncertainties using MCMC, terminating the chains when the interensemble Gelman–Rubin (GR) statistic was less than 1.003. For K2-19b, we measured a mass of $33 \pm 5 M_\oplus$. The RVs were insufficient

to detect planets c or d, but we placed upper limits on their masses of $M_{p,c} < 10.2 M_\oplus$ and $M_{p,d} < 3.5 M_\oplus$ at 95% confidence.

We found that η_1 , the amplitude of the quasiperiodic RV variability included in our GP noise model, was $7.4 \pm 2.2 \text{ m s}^{-1}$, in agreement with our previous estimate. This value is comparable to reflex velocity of planet b, and it underscores the importance of treating spot-induced RV-variability in the RV analysis. We recommend that future RV campaigns targeting K2-19 (or similar stars) observe at high cadence to better trace this quasiperiodic noise source.

We explored fits where e_b and ω_b were allowed to vary. However, this additional model complexity was disfavored by the BIC, with $\Delta\text{BIC} = -5$. Therefore, the RVs alone are insufficient to detect eccentricity for K2-19b. We characterized the values of e_b excluded solely by the RVs by running a second MCMC where $\sqrt{e_b} \cos \omega_b$ and $\sqrt{e_b} \sin \omega_b$ were allowed to vary. We found that $e_b < 0.27$ at 95% confidence, which is consistent with our photodynamical analysis presented in Section 4.2.

We note that our RV-only mass measurement of planet b is inconsistent at the $\sim 3\sigma$ level with that of Nespral et al. (2017), who reported $M_{p,b} = 54.8 \pm 7.5 M_\oplus$. The Nespral et al. (2017) analysis used 22 RVs from three different instruments: FIES, HARPS-N, and HARPS. We hypothesize that, in the Nespral et al. (2017) analysis, biases due to stellar activity were amplified given the sparse sampling of the RV timeseries and offsets between the RV data sets.

As we show in Section 4.2, the constraints from TTVs on the masses and eccentricities of K2-19b and c are more precise than those from the RVs. However, the RVs provide sensitivity to nontransiting planets that could compromise the accuracy of the TTV model. Nontransiting planets near first-order MMR are the most concerning, as they would produce the largest TTVs.

To search for such planets, we computed the Lomb–Scargle periodogram (Lomb 1976; Scargle 1982) of the residuals to the most probable Keplerian model (see Figure 5). We found no additional signals with a bootstrap false alarm probability of $< 10\%$ (VanderPlas 2018). Detection of an exoplanet from RVs alone with P less than the observing baseline generally requires $K \gtrsim \alpha \sigma_{\text{RV}} / \sqrt{N_{\text{obs}}}$, where σ_{RV} is the individual RV measurement uncertainty and α is a numerical prefactor of ≈ 10 (Howard & Fulton 2016). Adopting $\sigma_{\text{RV}} = 9 \text{ m s}^{-1}$, the quadrature sum of the two dominant noise terms, σ_{jit} and η_1 , we found that a planet with $K \gtrsim 13 \text{ m s}^{-1}$ would have been detectable. Therefore, at orbital periods comparable to those of K2-19b and c, the RVs rule out planets with masses comparable to K2-19b. This supports the assumption in our photodynamical model that the TTV signal is dominated by interactions between K2-19b and K2-19 c.

4.2. Photodynamical Analysis

To extract the information contained in both the RV and photometric data sets, we performed a photodynamical analysis. We used the Phodymm code, which is described in Mills et al. (2016). Given an initial configuration, Phodymm performs an N -body integration and forward models the light curve. The forward modeling approach has the advantage that it naturally handles simultaneous transits (Pál 2008) and simultaneously models all transit characteristics such as duration and depth variations, compared to other techniques that model derived transit times (see, e.g., TTVFast; Deck et al. 2014).

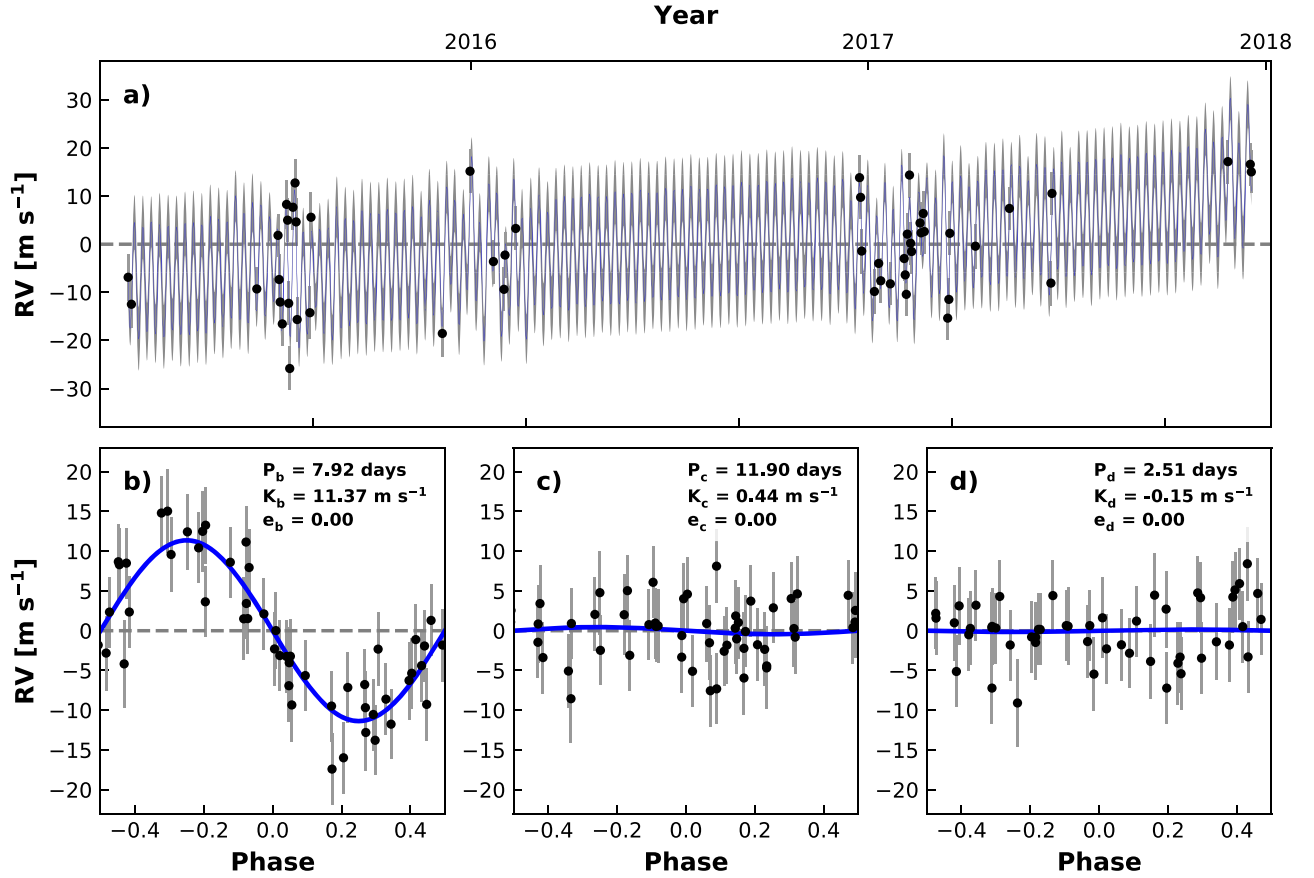


Figure 5. The three-Keplerian fit to the K2-19 radial velocities (RVs), assuming circular orbits (see Section 4.1). Panel (a): points show RVs from HIRES and the line shows the most probable Keplerian model. The gray band shows the Gaussian process model that accounts for quasiperiodic correlated noise due to starspots. Panel (b) shows the phase-folded RVs and the most probable Keplerian model for K2-19b with contributions from the GP noise model, dv/dt term, and other Keplerians removed. Panel (c), same as (b), but for K2-19 c. Panel (d), same as (b), but for K2-19d.

For each planet, we specified an initial set of osculating elements: P , T_c , e , ω , i , and Ω . Here, i is the inclination and Ω is the longitude of ascending node. The model also requires M_p and R_p/R_* for each planet, as well as stellar parameters, M_* and R_* , and quadratic limb-darkening parameters, q_1 and q_2 .

Because Ω is defined with respect to an arbitrary reference direction, we may fix Ω_b to 0° without loss of generality. K2-19d is dynamically decoupled from K2-19b and c and does not significantly affect the transits of the other planets gravitationally. However, K2-19d sometimes transits at the same time as K2-19b or c and therefore must be modeled out. We fixed $e_d = 0$, $\omega_d = 0^\circ$, and $\Omega_d = 0^\circ$. Following the recommendations of Eastman et al. (2013), for planets b and c, we parameterized $\{e, \omega\}$ as $\{\sqrt{e} \cos \omega, \sqrt{e} \sin \omega\}$, which enforces a uniform prior on e . In total, our model had 24 free parameters.

To assess the degree to which our model fits the K2 photometry, we defined

$$\chi_{\text{phot}}^2 = \sum_i \left(\frac{f_{\text{mod},i} - f_i}{\sigma_i} \right)^2,$$

where $f_{\text{mod},i}$, f_i , and σ_i are the modeled flux, observed flux, and flux uncertainty of the i th K2 observation.

For the *Spitzer* and ground-based transits, we modeled the derived transit times (Table 1) rather than the photometry directly because it is impractical to marginalize over the various systematic noise models that were used to derive the transit

times. We defined the following goodness-of-fit statistic:

$$\chi_{\text{times}}^2 = \sum_j \left(\frac{T_{c,\text{mod},j} - T_{c,j}}{\sigma_j} \right)^2,$$

where $T_{c,\text{mod},j}$, $T_{c,j}$, and σ_j are the modeled midpoint, observed midpoint, and timing uncertainty of the j th transit. Our final adopted log-likelihood is

$$\log \mathcal{L} = -\frac{1}{2} \chi_{\text{phot}}^2 - \frac{1}{2} \chi_{\text{times}}^2.$$

Following Petigura et al. (2018a), we incorporated the RV mass constraints as Gaussian priors on the planet masses. We checked that this treatment is justified by verifying that the posteriors on K_1 , K_2 , and K_3 (Section 4.1) are Gaussian and uncorrelated. Finally, we applied Gaussian priors on M_* and R_* based on our stellar characterization (see Table 3).

We explored the range of plausible models using Differential Evolution MCMC (DEMC). We ran 40 walkers and checked for convergence by periodically computing the GR statistic (Gelman & Rubin 1992). We terminated our runs after 80,000 steps, when the GR statistic was less than 1.05 for all parameters. After inspecting the chains, we discarded the first 10,000 steps as burn-in.

Figure 2 shows the MAP photodynamical fit to the K2 data set. We note that there is increased scatter in the residuals during transits due to spot crossing events. These spot crossings

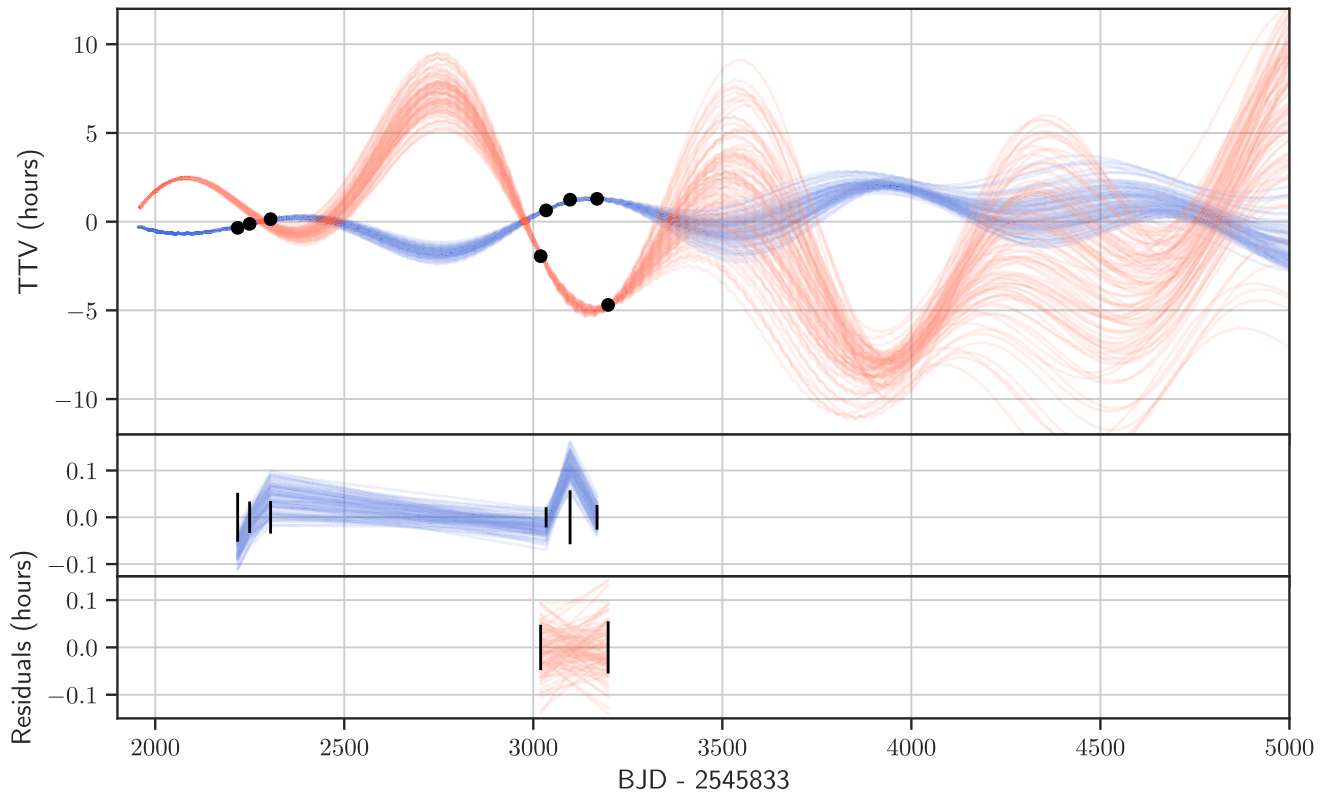


Figure 6. Top: black points show measured transit times with respect to a reference linear ephemeris. Blue and orange lines show transit times of K2-19b and c, respectively, computed from 100 draws from our MCMC chains (see Section 4.2). We do not show times from the *K2* epoch ($t = 1980\text{--}2060$ days) because we model the flux timeseries directly. The lines in the bottom panels represent the residuals to the predicted transit times and the formal timing uncertainties. Most of the model draws are within 2σ of the measured transit times and indicate good agreement between data and model.

do not systematically bias the model fits because they occur randomly over the transit chords. Figure 6 shows 100 representative draws from the chains that illustrate the range of allowed transit times. The dominant TTV pattern is sinusoidal with $P' \approx 800$ days, but other harmonics are visible. To facilitate future observations of these planets we have included our predicted transit times 2029 in the Appendix.

The planet parameters are summarized in Table 3. We have included the joint posterior distributions for all parameters along with a discussion of several noteworthy covariances in the Appendix. We found that K2-19b and c are $32.4 \pm 1.7 M_{\oplus}$ and $10.8 \pm 0.6 M_{\oplus}$, respectively.

While TTVs and RVs in principle provide complementary information, in our case, the TTVs are far more constraining. As an experiment, we ran the photodynamical model with no RV mass priors. The mass and eccentricity constraints are all consistent to within 2σ . In particular, photometry alone yields $M_{p,c} = 30.7 \pm 1.5 M_{\oplus}$. We note that K2-19 c is one of roughly a dozen planets with independent mass constraints from TTVs and RVs. See Mills & Mazeh (2017) for further discussion and a comparison of the two techniques.

We show the constraints on the planets' eccentricity vectors ($e \cos \omega$, $e \sin \omega$) in Figure 7. Both K2-19b and c have moderate eccentricities of $e_b = 0.20 \pm 0.03$ and $e_c = 0.21 \pm 0.03$ and well-aligned apsides $\omega_c - \omega_b = 2^\circ \pm 2^\circ$. The eccentricities and orbital alignment of these two planets have important implications for formation history and their present-day dynamics, which we discuss in Section 6.

Previously, Barros et al. (2015) measured masses and eccentricities of $M_{p,b} = 44 \pm 12 M_{\oplus}$ and $M_{p,c} = 16.9^{+7.7}_{-2.8} M_{\oplus}$

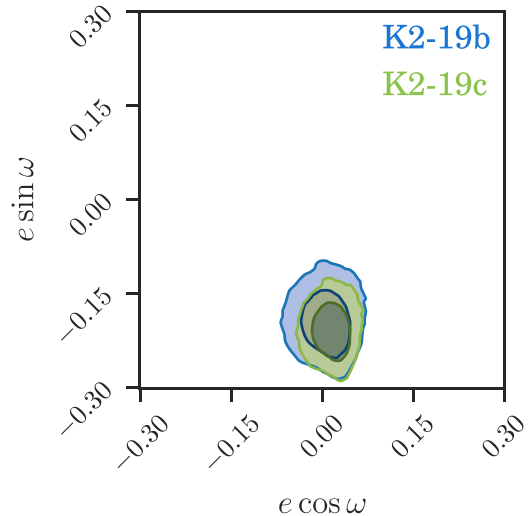


Figure 7. 2D joint posterior of $e \cos \omega$ and $e \sin \omega$ for K2-19b (blue) and K2-19c (green); the contours show 1σ and 2σ levels. The eccentricities of both planets (i.e., the radial distance from the origin) are nonzero and are consistent to within errors, $e_b = 0.20 \pm 0.03$ and $e_c = 0.21 \pm 0.03$. The planets have well-aligned apsides with $\Delta\omega = 2 \pm 2(\text{deg})$.

and $e_b = 0.119^{+0.082}_{-0.035}$ and $e_c = 0.095^{+0.073}_{-0.035}$ using just the *K2* photometry and three ground-based transits of K2-19b. Our measurements are consistent with those of Barros et al. (2015) at the $1\text{--}2\sigma$ level, but our measurements have smaller uncertainties on all parameters due to the additional *Spitzer* transits.

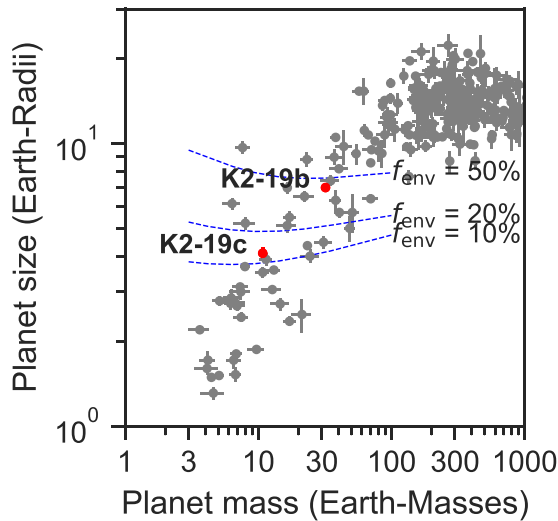


Figure 8. K2-19 planets viewed in context with other exoplanets. Gray points show the masses and radii of exoplanets where mass is measured to 25% or better. The K2-19 planets are shown in red and the uncertainties are comparable to the point size. The blue lines show mass–radius relationships for model planets having an Earth-composition core and various envelope fractions of H/He, $f_{\text{env}} = M_{\text{env}}/M_p$.

5. Core/Envelope Structure

Here, we examine the K2-19 planets in the context of other known exoplanets. Figure 9 shows a mass–radius diagram constructed from the NASA Exoplanet Archive (Akeson et al. 2013). Our $\sim 5\%$ mass measurements are among the most precise for any sub-Jovian size planet. Mass and radius reflect a planet’s core/envelope distribution. K2-19 are both “sub-Saturns,” which we define as planets with $R_p = 4\text{--}8 R_{\oplus}$. The bulk composition of sub-Saturns may be well-approximated by a two-component model consisting of a high density core and a H/He envelope of solar composition (Lopez & Fortney 2014; Petigura et al. 2016). For sub-Saturns, their total size is determined largely by their envelope fraction $f_{\text{env}} = M_{\text{env}}/M_p$, and thus changes in the detailed core composition weakly affect the total size.

Lopez & Fortney (2014) computed planet radii over a grid of M_p , f_{env} , age, and incident flux S_{inc} . As a point of reference, we show the mass–radius relationship for these models at several values of f_{env} in Figure 8.¹⁹ Both K2-19b and c require volumetrically significant envelopes to explain their masses and sizes. Following Petigura et al. (2017), we derived core masses and envelope fractions for these planets by interpolating over the Lopez & Fortney (2014) model grid. K2-19c has a core mass of $9.4 \pm 0.5 M_{\oplus}$ and is $14\% \pm 1\%$ envelope by mass, while K2-19b has a core mass of $18 \pm 1 M_{\oplus}$ and is $44\% \pm 3\%$ envelope by mass.

Petigura et al. (2017) compiled a sample of 23 sub-Saturns with well-measured masses and radii to examine trends within this population. One trend is that sub-Saturns have a range of envelope fractions, and that range broadens with decreasing equilibrium temperature. This broadening is likely due to the decreasing importance of photoevaporation at lower T_{eq} . As shown in Figure 9, the K2-19 planets have intermediate T_{eq} of ~ 800 K and span the full range of f_{env} .

¹⁹ Formally, we set age = 5 Gyr and $S_{\text{inc}} = 80 S_{\oplus}$ in order to plot single lines, but we note that these curves are nearly overlapping at low S_{inc} and late times.

Petigura et al. (2017) also noted a positive correlation between the host star metallicity and the total mass of sub-Saturns. As intermediate mass sub-Saturns around a near solar-metallicity star, the K2-19 planets also conform to this trend. The emerging M_p –[Fe/H] correlation may point to metallicity dependent effects in the growth of cores and/or accretion of gas from the protoplanetary disk. However, an expanded sample size is needed to more thoroughly assess the significance of this correlation and possible dependencies on quantities like stellar mass, which is covariant with metallicity.

With $f_{\text{env}} = 44\% \pm 3\%$, K2-19b is one of the most envelope-rich sub-Saturns known. Its envelope fraction is nearly as high as K2-24c with $f_{\text{env}} = 52^{+5}_{-3}\%$ (Petigura et al. 2018a). Like K2-24c, K2-19b presents an intriguing challenge to traditional core-accretion theory. As a point of reference, in the canonical core-accretion models of Pollack et al. 1996, Saturn forms first as a $\approx 12 M_{\oplus}$ core that accretes H/He from the protoplanetary disk. At the crossover mass (i.e., when $M_{\text{env}} \approx M_{\text{core}}$ or when $f_{\text{env}} \approx 50\%$), runaway accretion begins and Saturn quickly grows to its final mass.

One could attempt to resolve the $f_{\text{env}} \approx 50\%$ problem by imagining that the disk dissipated right as K2-19b approached the runaway phase. While this scenario is impossible to rule out, it requires special timing of planet formation and is thus a priori unlikely. More likely, the inferred structure of K2-19b points to an incomplete understanding of core-nucleated accretion and motivates further theoretical explanations of planet conglomeration in the sub-Saturn mass regime.

6. Mean-motion Resonance

K2-19b and c are clearly near the 3:2 mean-motion resonance, but are they actually in resonance? Resonance requires the libration of a resonant angle, e.g.,

$$\phi = 3\lambda_c - 2\lambda_b - \varpi,$$

where λ is the mean longitude and ϖ is the longitude of periastron for either planet b or c. Librating angles are confined to a particular range while circulating angles sweep out all values between 0 and 2π . If ϕ is librating,

$$\langle \dot{\phi} \rangle = 3n_c - 2n_b - \dot{\varpi} = 0.$$

We simulated the plausible long-term evolution of K2-19b and c by taking 100 draws from the posterior samples from Section 4.2 and evolving them for 50 yr using the IAS15 N -body integrator included in the REBOUND package (Rein & Liu 2012; Rein & Spiegel 2015).

Our integrations all revealed the same qualitative apsidal outcome: circulation rather than libration of $\langle \phi \rangle$. In Figure 10, we show the evolution of ϕ for a representative simulation. The quantity $3n_c - 2n_b$ has a time average of -0.003 rad day⁻¹, much larger than $\dot{\varpi}_b$ or $\dot{\varpi}_c$. Instead, the planet eccentricities evolve secularly over a period of roughly six years while the apsides remain aligned.

In our simulations we did not include precession from general relativity or the quadrupole field due to K2-19d. Here, we justify these approximations. Planet b experiences apsidal precession due to an effective quadrupole moment from planet d. The rate of this precession is given by

$$\dot{\omega}_{J_2} = 3n_b J_2 \left(\frac{a_d}{a_b} \right)^2$$

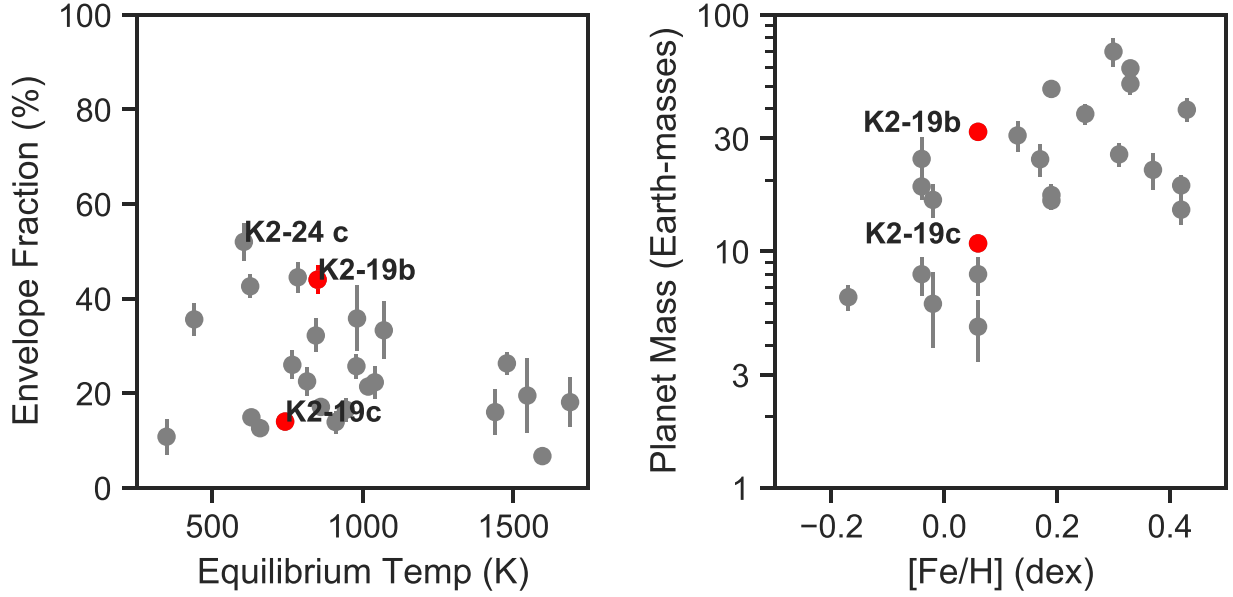


Figure 9. K2-19 planets viewed in context among other sub-Saturns ($R_p = 4\text{--}8 R_{\oplus}$). Left: envelope fraction vs. equilibrium temperature. Gray points are drawn from Petigura et al. (2017). The K2-19 planets straddle the range of observed envelope fractions. K2-19b resides near the upper envelope of the f_{env} distribution, which broadens toward lower T_{eq} . Right: same sample as left, but showing planet mass vs. host star metallicity. There is a positive correlation between $[\text{Fe}/\text{H}]$ and M_p , with significant scatter. The K2-19 planets conform to this trend.

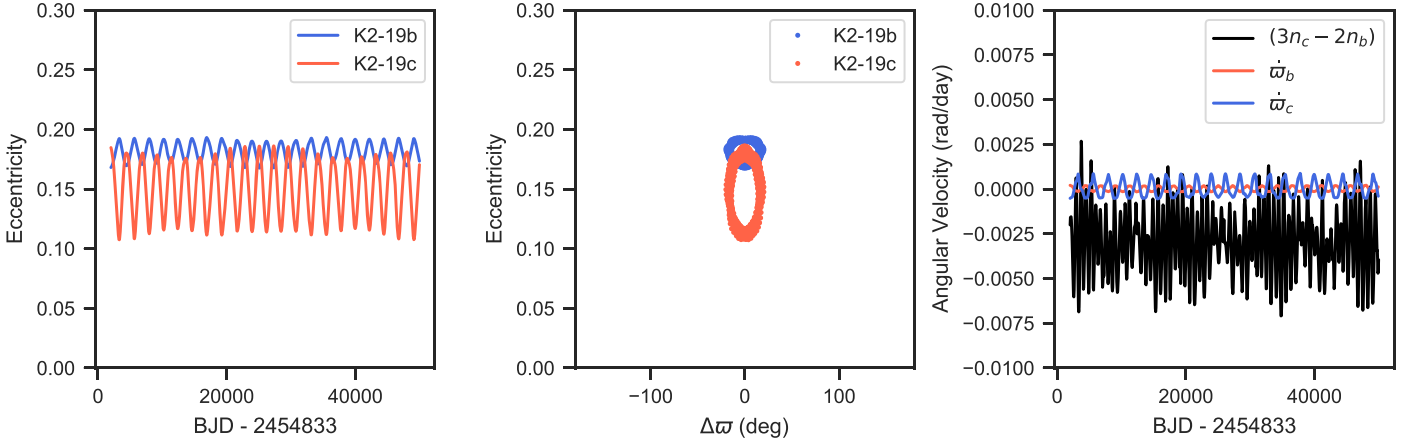


Figure 10. Dynamical evolution of a representative solution from our photodynamical model, based on a 50 yr N -body integration. Left: eccentricity as a function of time. The planets exchange eccentricity over a secular timescale of ~ 6 yr. Middle: same simulation as left, but with $\Delta\omega$ on the x -axis. The planets precess together and retain apsidal alignment. Right: several angular velocities relevant to the planet's resonant state. Because the quantity $3n_c - 2n_b - \dot{\omega}$ does not have a time average of zero for either $\dot{\omega}_b$ or $\dot{\omega}_c$, the planets are not in the 3:2 mean-motion resonance. Instead, the resonant angles circulate at a rate of ~ 1 radian per year.

where

$$J_2 = \frac{1}{2} \frac{m_d}{M_*}.$$

We find that

$$\tau_{J_2} = 2\pi/\dot{\omega}_{J_2} \approx 2 \times 10^4 \text{ yr.}$$

K2-19b also experiences apsidal precession due to GR with a rate of

$$\dot{\omega}_{\text{GR}} = 3n_b \frac{GM_*}{a_b c^2}$$

so that

$$\tau_{\text{GR}} = 2\pi/\dot{\omega}_{\text{GR}} \approx 6 \times 10^4 \text{ yr.}$$

Because τ_{GR} and τ_{J_2} are much longer than the secular eccentricity oscillations, we are justified in neglecting their effects above.

7. Formation

An intriguing aspect of the K2-19 system is that both the physical and orbital characteristics of planets b and c are peculiar, especially when viewed against the backdrop of other well-characterized planetary systems, including our own. In particular, from the perspective of conventional planet formation theory (Armitage 2013), the inferred properties of the K2-19 planets present a formidable challenge. As already mentioned above, the near-unity envelope-to-core mass fraction of K2-19 c is not a natural outcome of the core-nucleated accretion model of planet formation (Pollack et al. 1996; Hubickyj et al. 2005).

However, even if we ignore the physical structure of these planets altogether, their orbital architecture lies in sharp contrast with theoretical expectations (Kley & Nelson 2012).

The most noteworthy feature of the K2-19bc pair is their proximity to exact 3:2 mean-motion commensurability. In general, orbital resonances have long been recognized as an aftereffect of convergent orbital migration (Tanaka et al. 2002; Bitsch et al. 2015). Furthermore, theoretical treatment of migration predicts that planets as massive as K2-19b and c should have readily experienced disk-driven orbital decay. Therefore, it is not unreasonable to anticipate a distinctly resonant present-day architecture of K2-19 that could in turn be attributed to a migratory origin. Moreover, coupled with long-range migration, resonant interactions are well-known to adiabatically excite the orbital eccentricities of the constituent planets (see, e.g., Burns & Matthews 1986; Malhotra 1995; Lee & Peale 2002), and our photodynamical model revealed significant eccentricities of $e \approx 0.2$. Nevertheless, as we showed in Section 6, the system is incompatible with mean-motion resonance, and thus the entire aforementioned narrative.

Both the values of the eccentricities themselves, as well as the apsidal orientations of the orbits are contradictory to those that would have been sculpted by convergent migration. More specifically, within the framework of the standard resonance capture scenario, orbital eccentricities are determined by a balance between adiabatic excitation that arises from convergent orbital evolution and disk-driven eccentricity damping. Quantitatively, this balance yields eccentricities of $e \sim h/r \sim 0.05$, where h is the disk scale height and r is the distance to the host star (Pichierri et al. 2018). However, the inferred eccentricities of K2-19b and c exceed this characteristic value by a factor of a few. More dramatically, a clear consequence of adiabatic resonance capture is the antialignment of planetary apsidal lines, such that $\Delta\varpi \approx 180^\circ$ (Batygin & Morbidelli 2013a). Instead, in this system, the data clearly points to apsidal alignment, characterized by $\Delta\varpi \approx 0^\circ$. It is this requirement for the periape alignment that prevents us from finding a suitable resonant solution for the planetary orbits.

To elaborate on apsidal alignment further, we note that stable resonant equilibria that exist far away from $\Delta\varpi \approx 180^\circ$ are indeed possible at sufficiently high eccentricities (Beaugé et al. 2006). In an effort to consider this possibility for K2-19, we carried out an N -body numerical experiment, simulating the convergent migration and subsequent resonant locking of K2-19b and c. In particular, we initialized both planets on circular orbits, at a period ratio 20% outside of nominal 3:2 commensurability and computed the orbital evolution resulting from mutual gravitational perturbations as well as a fictitious force designed to mimic planet–disk interactions. The integration was carried out using the Bulirsch–Stoer algorithm (Press et al. 1992), with an accuracy parameter set to 10^{-10} .

We adopted the model disk acceleration formulae spelled out in Papaloizou & Larwood (2000), setting the convergent migration timescale $\tau_a = 2 \times 10^4$ yr. While our choice of τ_a was arbitrary, the resulting evolution is adiabatic and thus insensitive to the adopted τ_a (Henrard 1982). To prevent the system from equilibrating in resonance with low eccentricities (e.g., Pichierri et al. 2017), we unphysically set the timescale for eccentricity damping to $\tau_e = \infty$, such that disk-driven convergent migration resulted in continued adiabatic enhancement of the planetary eccentricities once a resonant coupling was established (Lee 2004).

The initial results of our simulations followed a familiar pattern: the planets migrated convergently, were captured into the 3:2 mean-motion resonance, and developed finite eccentricities while locked into strict apsidal antialignment with $\Delta\varpi = 180^\circ$. Once the planetary eccentricities reached sufficiently large values, however, we observed deviations away from exact apsidal antialignment. Nevertheless, we found that in order to attain $\Delta\varpi$ even remotely close to zero, unreasonably large eccentricities were required. For example, a resonant equilibrium at $\Delta\varpi \sim 60^\circ$ requires $e > 0.8$ for both planets. Thus, our results show that although asymmetric equilibria can follow after capture into mean-motion resonance, the required eccentricities are simply too high to be observationally permissible. Indeed, resonant coupling appears to be strictly ruled out by the available data.²⁰

For completeness, we can also speculate regarding an alternative mechanism for finite eccentricity excitation: mean-motion resonance crossing due to divergent migration. In this scenario, planets start out interior to a resonant period ratio and cross a commensurability, which results in a noncapturing encounter with the resonant separatrix. This yields an impulsive excitation of the planetary eccentricities. For example, models of the early solar system by Tsiganis et al. (2005), planetesimal scattering by Jupiter and Saturn leads to divergent migration, and the crossing of the 2:1 resonance excites eccentricities of $\approx 5\%–10\%$. This scenario, however, also yields strict apsidal antialignment after the encounter (Batygin & Morbidelli 2013a) and is therefore also ruled out by the observations.

We conclude this section with a brief remark on dynamical stability and its relationship to the observed orbital architecture of the K2-19 system. A trivial examination of the derived orbital elements illustrates that this system is strongly AMD-unstable (Petit et al. 2018). So how is the stability of these planets ensured? It is well known that highly eccentric planets or satellites locked into orbital commensurabilities often derive long-term orbital stability from the resonant phase-protection mechanism. As we have demonstrated above, however, in the case of K2-19b and c, liberation of resonant angles appears to be forbidden by the observational data. Instead, the planets around K2-19 appear to be protected from close encounters primarily by the fact that the orbits have persistently colinear apses and are therefore geometrically nested. While this configuration is indeed long-term stable, the dynamical genesis of this orbital configuration remains elusive.

8. Conclusions

The K2-19 system offers a sharp contrast to the architecture and physical properties of the solar system planets. In the solar system, not a single planet resides interior to Mercury ($P = 88$ days), while for K2-19 there are (at least) three planets with $P < 12$ days. K2-19c straddles a gap in the size distribution of solar system planets between the ice giants and Jovians. Finally, no pair of major solar system planets resides so close to mean-motion resonance, although numerous Kuiper Belt objects are in resonance with Neptune, of which Pluto is the prototypical example.

²⁰ As a corollary, we note that orbits which originate in resonance can be driven out of exact commensurability while maintaining liberation of resonant angles by long-term energy dissipation (Lithwick & Wu 2012; Batygin & Morbidelli 2013b). This scenario, however, is only relevant to systems with vanishingly low eccentricities and period ratios well outside of the nominal resonance width, both of which are not satisfied in K2-19.

The planets orbiting K2-19 are also unusual compared to typical extrasolar planets. Highly irradiated planets between the size of Neptune and Saturn are rare: Petigura et al. (2018b) performed a demographic analysis of GK stars observed by *Kepler* and found 0.36 planets per 100 stars with $R_p = 4\text{--}8 R_\oplus$ and $P < 10$ days. In addition, such proximity to resonance is not a common feature of extrasolar planets; to first order, planet period ratios are uniformly distributed (Lissauer et al. 2011).

Motivated by the unusual characteristics of the K2-19 planets, our team collected RVs with Keck/HIRES and additional photometry from *Spitzer* and LCO. The RV data set was sufficient to detect the reflex motion due to K2-19b at 7σ . However, the RVs alone were insufficient to detect K2-19c due to its lower mass. Quasiperiodic RV variability due to spots of $\approx 7 \text{ m s}^{-1}$ limited the sensitivity of the RV data set. Spot contrasts are smaller at redder wavelengths, and K2-19 would benefit from RV monitoring in the NIR by instruments such as IRD (Kotani et al. 2018).

The high precision of the *K2* and *Spitzer* photometry combined with our multiyear time baseline provided much more stringent constraints on the physical and orbital properties of the planets. We measured the masses of both K2-19b and c to $\approx 5\%$, which are among the most precise of any sub-Jovian exoplanet. Our mass and radius measurements provided a window into the core-envelope structure of these planets. We found that K2-19c is roughly 15% envelope by mass, while K2-19b is nearly 50%—close to the canonical crossover mass leading to runaway accretion (Pollack et al. 1996). These planets contribute to an emerging picture of planets between the size of Neptune and Saturn: where cores of a given mass exhibit a wide diversity of envelope fractions and where that diversity grows with decreasing irradiation (see Figure 9).

Through our photodynamical analysis, we found that these planets have moderate eccentricities of ≈ 0.2 and aligned apsides. The planets are experiencing rapid secular eccentricity oscillations with a ≈ 6 yr timescale, but the system is currently not in mean-motion resonance. Moreover, the system’s present configuration presents a challenge to formation pathways that involve mean-motion resonance in the past. Scenarios where the system passes through the 3:2 resonance from above or below predict antialigned apsides, which are ruled out by the data. Future photometric or RV monitoring would shed additional light on this enigmatic system.

We thank the anonymous reviewer for helpful suggestions that improved this manuscript.

E.A.P. acknowledges support for this work by NASA through the NASA Hubble Fellowship grant *HST-HF2-51417* awarded by the Space Telescope Science Institute, which is operated by the Association of Universities for Research in Astronomy, Inc., for NASA, under contract NAS5-26555. S.C. C.B. acknowledges support from Fundação para a Ciência e a Tecnologia (FCT) through Investigador FCT contract IF/01312/2014/CP1215/CT0004 and by FEDER through COMPETE2020 and POCI in the framework of the project POCI-01-0145-FEDER-028953.

This work made use of NASA’s Astrophysics Data System Bibliographic Services.

This work is based in part on observations made with the *Spitzer Space Telescope*, which is operated by the Jet Propulsion Laboratory, California Institute of Technology under a contract with NASA. Support for this work was provided by NASA through an award issued by JPL/Caltech. This work makes use of observations from the LCOGT network.

Some of the data presented herein were obtained at the W. M. Keck Observatory, which is operated as a scientific partnership among the California Institute of Technology, the University of California, and NASA. The authors wish to recognize and acknowledge the very significant cultural role and reverence that the summit of Maunakea has always had within the indigenous Hawaiian community. We are most fortunate to have the opportunity to conduct observations from this mountain.

Facilities: *Kepler*, *Spitzer*, Keck:I (HIRES), LCOGT.

Software: batman (Kreidberg 2015), emcee (Foreman-Mackey et al. 2013), Phodimm (Mills et al. 2016), REBOUND (Rein & Liu 2012), EVEREST2.0 (Luger et al. 2018), RadVel (Fulton et al. 2018).

Appendix Photodynamical Model

Here, we include some supplemental information regarding our photodynamical model described in Section 4.2. Table 4 lists the predicted transit times and uncertainties for K2-19b and c up to 2029. Figure 11 shows the 2D joint posteriors of all parameters included in our photodynamical model.

We highlight the covariances between mass and eccentricity in Figure 12. The masses of planets b and c are correlated because the amplitudes of near-resonant TTVs constrain planet mass ratios (Lithwick et al. 2012). However, the RVs and higher order TTV terms (i.e., chopping) constrain the individual masses directly (Deck & Agol 2015). Figure 12 also illustrates a positive correlation between $e_b \cos \omega_b$ and $e_c \cos \omega_c$ and between $e_b \sin \omega_b$ and $e_c \sin \omega_c$. This is another common feature of near-resonant systems: the TTV amplitude and phase encodes linear combinations of $e \cos \omega$ and $e \sin \omega$ (Lithwick et al. 2012).

Table 4
Predicted Transit Times

Planet	i	UTC date	T_c days	$\sigma(T_c)$ days
b	0	2014 Jun 4	1980.3840	0.0002
c	0	2014 Jun 8	1984.2722	0.0008
b	1	2014 Jun 12	1988.3041	0.0002
c	1	2014 Jun 20	1996.1834	0.0006
b	2	2014 Jun 20	1996.2220	0.0002
c	476	2029 Dec 11	7648.8365	0.1814
b	716	2029 Dec 14	7651.5243	0.0468
b	717	2029 Dec 21	7659.4466	0.0446
c	477	2029 Dec 23	7660.7298	0.1710
b	718	2029 Dec 29	7667.3662	0.0434

Note. Predicted transit times for K2-19b and c, where i , is an index that labels individual transits. Times are given in $\text{BJD}_{\text{TDB}} - 2454833$.

(This table is available in its entirety in machine-readable form.)

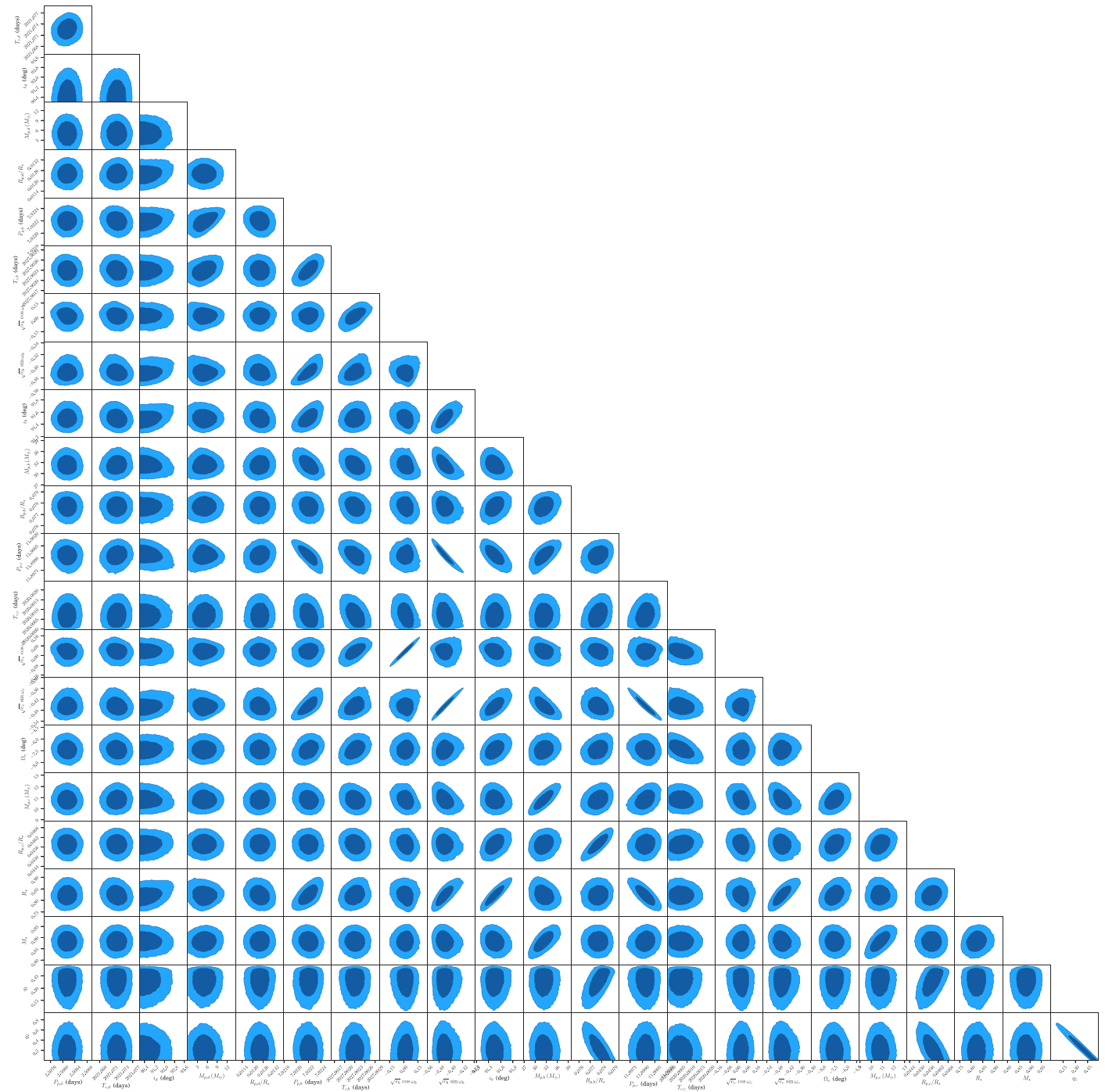


Figure 11. 2D joint posterior probability distributions for our photodynamical model (Section 4.2). The dark and light regions show 1σ and 2σ contours, respectively.

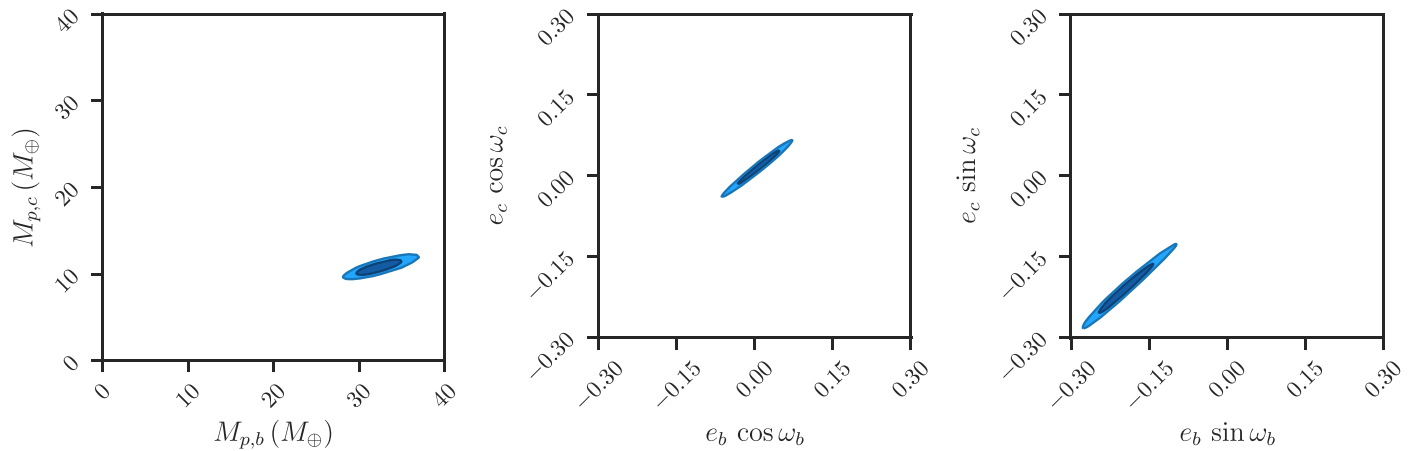


Figure 12. Same as Figure 11, but highlighting several noteworthy covariances between planet masses and planet eccentricities. Left panel: constraint on $M_{p,b}$ and $M_{p,c}$. The covariance between the planet masses is typical of TTV analyses which tend to provide smaller fractional uncertainties on mass ratios than on individual masses. Middle panel: same as left but for $e_b \cos \omega_b$ and $e_c \cos \omega_c$. The covariance results from the fact that TTVs constrain linear combinations of the eccentricity vectors. Right panel: same as the middle but for $e_b \sin \omega_b$ and $e_c \sin \omega_c$.

ORCID iDs

Erik A. Petigura <https://orcid.org/0000-0003-0967-2893>
 John Livingston <https://orcid.org/0000-0002-4881-3620>
 Sean M. Mills <https://orcid.org/0000-0002-4535-6241>
 Howard Isaacson <https://orcid.org/0000-0002-0531-1073>
 Benjamin J. Fulton <https://orcid.org/0000-0003-3504-5316>
 Andrew W. Howard <https://orcid.org/0000-0001-8638-0320>
 Lauren M. Weiss <https://orcid.org/0000-0002-3725-3058>
 Néstor Espinoza <https://orcid.org/0000-0001-9513-1449>
 Daniel Jontof-Hutter <https://orcid.org/0000-0002-6227-7510>
 Avi Shporer <https://orcid.org/0000-0002-1836-3120>
 Daniel Bayliss <https://orcid.org/0000-0001-6023-1335>

References

- Aigrain, S., Pont, F., & Zucker, S. 2012, *MNRAS*, 419, 3147
 Akeson, R. L., Chen, X., Ciardi, D., et al. 2013, *PASP*, 125, 989
 Armitage, P. J. 2013, *Astrophysics of Planet Formation* (Cambridge: Cambridge Univ. Press)
 Armstrong, D. J., Santerne, A., Veras, D., et al. 2015, *A&A*, 582, A33
 Barros, S. C. C., Almenara, J. M., Demangeon, O., et al. 2015, *MNRAS*, 454, 4267
 Batygin, K., & Morbidelli, A. 2013a, *A&A*, 556, A28
 Batygin, K., & Morbidelli, A. 2013b, *AJ*, 145, 1
 Beaugé, C., Michtchenko, T. A., & Ferraz-Mello, S. 2006, *MNRAS*, 365, 1160
 Benneke, B., Werner, M., Petigura, E., et al. 2017, *ApJ*, 834, 187
 Bitsch, B., Lambrechts, M., & Johansen, A. 2015, *A&A*, 582, A112
 Brewer, J. M., Fischer, D. A., Valenti, J. A., & Piskunov, N. 2016, *ApJS*, 225, 32
 Brown, T. M., Baliber, N., Bianco, F. B., et al. 2013, *PASP*, 125, 1031
 Burns, J. A., & Matthews, M. S. (ed.) 1986, *Satellites* (Tucson, AZ: Univ. Arizona Press)
 Claret, A., Hauschildt, P. H., & Witte, S. 2012, *A&A*, 546, A14
 Dai, F., Winn, J. N., Albrecht, S., et al. 2016, *ApJ*, 823, 115
 Deck, K. M., & Agol, E. 2015, *ApJ*, 802, 116
 Deck, K. M., Agol, E., Holman, M. J., & Nesvorný, D. 2014, *ApJ*, 787, 132
 Deming, D., Knutson, H., Kammer, J., et al. 2015, *ApJ*, 805, 132
 Eastman, J., Gaudi, B. S., & Agol, E. 2013, *PASP*, 125, 83
 Foreman-Mackey, D., Hogg, D. W., Lang, D., & Goodman, J. 2013, *PASP*, 125, 306
 Fulton, B. J., & Petigura, E. A. 2018, *AJ*, 156, 264
 Fulton, B. J., Petigura, E. A., Blunt, S., & Sinukoff, E. 2018, *PASP*, 130, 044504
 Gaia Collaboration, Brown, A. G. A., Vallenari, A., et al. 2018, *A&A*, 616, A1
 Gelman, A., & Rubin, D. B. 1992, *StaSc*, 7, 457
 Goodman, J., & Weare, J. 2010, *CAMCS*, 5, 65
 Grunblatt, S. K., Howard, A. W., & Haywood, R. D. 2015, *ApJ*, 808, 127
 Haywood, R. D., Collier Cameron, A., Queloz, D., et al. 2014, *MNRAS*, 443, 2517
 Henrard, J. 1982, *CeMec*, 27, 3
 Howard, A. W., & Fulton, B. J. 2016, *PASP*, 128, 114401
 Howard, A. W., Johnson, J. A., Marcy, G. W., et al. 2010, *ApJ*, 721, 1467
 Howell, S. B., Sobek, C., Haas, M., et al. 2014, *PASP*, 126, 398
 Hubickyj, O., Bodenheimer, P., & Lissauer, J. J. 2005, *Icar*, 179, 415
 Ingalls, J. G., Krick, J. E., Carey, S. J., et al. 2012, *Proc. SPIE*, 8442, 84421Y
 Kipping, D. M. 2013, *MNRAS*, 435, 2152
 Kley, W., & Nelson, R. P. 2012, *ARA&A*, 50, 211
 Kotani, T., Tamura, M., Nishikawa, J., et al. 2018, *Proc. SPIE*, 10702, 1070211
 Kreidberg, L. 2015, *PASP*, 127, 1161
 Lee, M. H. 2004, *ApJ*, 611, 517
 Lee, M. H., & Peale, S. J. 2002, *ApJ*, 567, 596
 Lissauer, J. J., Ragozzine, D., Fabrycky, D. C., et al. 2011, *ApJS*, 197, 8
 Lithwick, Y., & Wu, Y. 2012, *ApJL*, 756, L11
 Lithwick, Y., Xie, J., & Wu, Y. 2012, *ApJ*, 761, 122
 Livingston, J. H., Crossfield, I. J. M., Werner, M. W., et al. 2019, *AJ*, 157, 102
 Lomb, N. R. 1976, *Ap&SS*, 39, 447
 Lopez, E. D., & Fortney, J. J. 2014, *ApJ*, 792, 1
 Luger, R., Kruse, E., Foreman-Mackey, D., Agol, E., & Saunders, N. 2018, *AJ*, 156, 99
 Malhotra, R. 1995, *AJ*, 110, 420
 Marcy, G. W., & Butler, R. P. 1992, *PASP*, 104, 270
 McCully, C., Volgenau, N. H., Harbeck, D.-R., et al. 2018, *Proc. SPIE*, 10707, 107070K
 Mills, S. M., Fabrycky, D. C., Migaszewski, C., et al. 2016, *Natur*, 533, 509
 Mills, S. M., & Mazeh, T. 2017, *ApJL*, 839, L8
 Narita, N., Hirano, T., Fukui, A., et al. 2015, *ApJ*, 815, 47
 Nespral, D., Gandolfi, D., Deeg, H. J., et al. 2017, *A&A*, 601, A128
 Pál, A. 2008, *MNRAS*, 390, 281
 Papaloizou, J. C. B., & Larwood, J. D. 2000, *MNRAS*, 315, 823
 Petigura, E. A., Benneke, B., Batygin, K., et al. 2018a, *AJ*, 156, 89
 Petigura, E. A., Howard, A. W., Lopez, E. D., et al. 2016, *ApJ*, 818, 36
 Petigura, E. A., Marcy, G. W., Winn, J. N., et al. 2018b, *AJ*, 155, 89
 Petigura, E. A., Sinukoff, E., Lopez, E. D., et al. 2017, *AJ*, 153, 142
 Petit, A. C., Laskar, J., & Boué, G. 2018, *A&A*, 617, A93
 Pichierrri, G., Morbidelli, A., & Crida, A. 2018, *CeMDA*, 130, 54
 Pichierrri, G., Morbidelli, A., & Lai, D. 2017, *A&A*, 605, A23
 Pollack, J. B., Hubickyj, O., Bodenheimer, P., et al. 1996, *Icar*, 124, 62
 Pont, F., Zucker, S., & Queloz, D. 2006, *MNRAS*, 373, 231
 Press, W. H., Teukolsky, S. A., Vetterling, W. T., & Flannery, B. P. 1992, *Numerical recipes in FORTRAN. The Art of Scientific Computing* (Cambridge: Cambridge Univ. Press)

- Rein, H., & Liu, S.-F. 2012, *A&A*, 537, A128
Rein, H., & Spiegel, D. S. 2015, *MNRAS*, 446, 1424
Scargle, J. D. 1982, *ApJ*, 263, 835
Schwarz, G. 1978, *AnSta*, 6, 461
Sinukoff, E., Howard, A. W., Petigura, E. A., et al. 2016, *ApJ*, 827, 78
Skrutskie, M. F., Cutri, R. M., Stiening, R., et al. 2006, *AJ*, 131, 1163
Tanaka, H., Takeuchi, T., & Ward, W. R. 2002, *ApJ*, 565, 1257
Tsiganis, K., Gomes, R., Morbidelli, A., & Levison, H. F. 2005, *Natur*, 435, 459
Valenti, J. A., Butler, R. P., & Marcy, G. W. 1995, *PASP*, 107, 966
VanderPlas, J. T. 2018, *ApJS*, 236, 16
Vaughan, A. H., Preston, G. W., & Wilson, O. C. 1978, *PASP*, 90, 267
Vogt, S. S., Allen, S. L., Bigelow, B. C., et al. 1994, *Proc. SPIE*, 2198, 362
Winn, J. N., Holman, M. J., Torres, G., et al. 2008, *ApJ*, 683, 1076